



# The CIV\* Survey: The Discovery of a CIV Dichotomy in the Circumgalactic Medium of L\* Galaxies

Samantha L. Garza<sup>1</sup> , Jessica K. Werk<sup>1</sup> , Trystyn A. M. Berg<sup>2</sup> , Yakov Faerman<sup>1</sup> , Benjamin D. Oppenheimer<sup>3</sup> ,  
Rongmon Bordoloi<sup>4</sup> , and Sara L. Ellison<sup>5</sup>

<sup>1</sup> Department of Astronomy, University of Washington, Seattle, WA 98195, USA; [samgarza@uw.edu](mailto:samgarza@uw.edu)

<sup>2</sup> National Research Council Herzberg Astronomy and Astrophysics, 5071 West Saanich Road, Victoria, BC, V8Z6M7, Canada

<sup>3</sup> University of Colorado, Center for Astrophysics and Space Astronomy, 389 UCB, Boulder, CO 80309, USA

<sup>4</sup> Department of Physics, North Carolina State University, Raleigh, NC 27695, USA

<sup>5</sup> Department of Physics and Astronomy, University of Victoria, Victoria, British Columbia, V8P 1A1, Canada

Received 2024 October 04; revised 2024 December 03; accepted 2024 December 03; published 2024 December 27

## Abstract

This paper investigates C IV absorption in the circumgalactic medium (CGM) of L\* galaxies and its relationship with galaxy star formation rates. We present new observations from the C IV in L\* galaxies survey (PID#17076) using the Hubble Space Telescope/Cosmic Origins Spectrograph. By combining these measurements with archival C IV data (46 observations total), we estimate detection fractions for star-forming ( $sSFR > 10^{-11} \text{ yr}^{-1}$ ) and passive galaxies ( $sSFR \leq 10^{-11} \text{ yr}^{-1}$ ) to be  $72_{-18}^{+14}\%$  [21/29] and  $23_{-15}^{+27}\%$  [3/13], respectively. This indicates a significant dichotomy in C IV presence between L\* star-forming and passive galaxies, with over 99% confidence. This finding aligns with J. Tumlinson et al., which noted a similar dichotomy in O VI absorption. Our results imply a substantial carbon reservoir in the CGM of L\* galaxies, suggesting a minimum carbon mass of  $\gtrsim 3.03 \times 10^6 M_{\odot}$  out to 120 kpc. Together, these findings highlight a strong connection between star formation in galaxies and the state of their CGM, providing insight into the mechanisms governing galaxy evolution.

*Unified Astronomy Thesaurus concepts:* [Galaxy evolution \(594\)](#); [Circumgalactic medium \(1879\)](#); [Quasar absorption line spectroscopy \(1317\)](#)

## 1. Introduction

The diffuse gaseous atmosphere surrounding the star-filled inner region of a galaxy is known as its circumgalactic medium (CGM). The CGM plays an essential role in a galaxy's evolution by hosting the gaseous reservoir that feeds the galaxy with gas, replenishing fuel for star formation and keeping a record of metal-enriched material ejected from the disk through winds and other feedback processes (N. Lehner & J. C. Howk 2011; M. S. Peeples et al. 2014; J. K. Werk et al. 2014; J. Tumlinson et al. 2017). The Hubble Space Telescope and the Cosmic Origins Spectrograph (HST/COS) have significantly advanced the study of the CGM over the past 15 yr, creating a compendium of gas around dwarf to L\* galaxies (e.g., J. K. Werk et al. 2013; R. Bordoloi et al. 2014; S. Borthakur et al. 2015; T. Heckman et al. 2017; T. A. M. Berg et al. 2018; N. Lehner et al. 2018), with additional focus on specific demographics such as starbursts (T. Heckman et al. 2017) and active galactic nuclei (AGN; T. A. M. Berg et al. 2018). However, many questions remain about how ongoing processes within galaxies impact the physical state of their CGM and vice versa. Quantifying the connection between these halos and their host galaxies can provide essential constraints on the coevolution of galaxies and the CGM.

Some progress has been made for the cool phase of the CGM ( $T \sim 10^4 \text{ K}$ ), where metal-enriched gas traced by Mg II has been used to compare the CGM content between star-forming and passive galaxies. The consensus is that the CGM of star-forming galaxies has higher Mg II equivalent widths and covering fractions than that of passive galaxies

(T.-W. Lan 2020; A. Anand et al. 2021). Mg II is often associated with star formation–driven winds (K. H. R. Rubin et al. 2014), showing a strong incidence rate along the minor axes of star-forming galaxies (R. Bordoloi et al. 2011). Other cool gas-phase tracers such as H I, Si II, and C III show no statistically significant correlation with galaxy star-forming properties (J. Tumlinson et al. 2013; J. K. Werk et al. 2013).

For the warm phase, a seminal result from the COS-Halos survey found a dichotomy in the content of O VI in the CGM of star-forming and passive galaxies (J. Tumlinson et al. 2011). O VI, a likely tracer of highly ionized  $T \sim 10^{5.5} \text{ K}$  gas, is abundant in the halos of actively star-forming L\* galaxies, while it is rarely found within 150 kpc of L\* passive galaxies (J. Tumlinson et al. 2011; S. D. Johnson et al. 2015; F. S. Zahedy et al. 2019). This dichotomy holds with greater than  $3\sigma$  significance for stellar mass–controlled samples of low-redshift ( $z < 0.6$ ) galaxies with  $10^{10.1} < M_{\star} < 10^{10.9}$  (K. Tchernyshyov et al. 2023).

While high ions and low ions likely trace distinct gas phases of the CGM and show different correlations with galaxy star-forming properties, it is unclear where intermediate ionization state gas tracers such as Si IV and C IV fit for L\* galaxies. For sub-L\* galaxies ( $\log M_{\star}/M_{\odot} \lesssim 10$ ), a tentative correlation was detected between C IV absorption strength and star formation, mirroring the dichotomy seen in O VI for L\* galaxies (R. Bordoloi et al. 2014). A similar case is probable for  $L \approx L^*$  galaxies, where these intermediate ions may trace warm photoionized material similar to low ions and/or may be produced in part by collisional ionization, either in equilibrium or out of equilibrium, for example, by turbulent mixing layers (e.g., K. Kwak & R. L. Shelton 2010). However, due to the wavelength coverage of available gratings on HST/COS, C IV and Si IV are rarely observed by CGM surveys prioritizing O VI, such as COS-Halos (J. K. Werk et al. 2013) and

**Table 1**  
CIViL\* Galaxy Sample Properties and C IV Measurements

Galaxy	$z_{\text{gal}}$	$z_{\text{qso}}$	sSFR ( $\log_{10} \text{yr}^{-1}$ )	$M_*$ ( $\log_{10} M_{\odot}$ )	$R_{\text{proj}}$ (kpc)	$R_{\text{proj}}/R_{200c}$	$M_{200c}$ ( $\log_{10} M_{\odot}$ )	$N_{\text{C IV}}$ ( $\log_{10} \text{cm}^{-2}$ )	References
(1)	(2)	(3)	(4)	(5)	(6)	(7)	(8)	(9)	(10)
J1427+2629_45940	0.0330	0.364	-12.0	10.4	170	1.07	11.6	< 13.14	COS-GASS
J1502+0649_41743	0.0460	0.288	-10.2	10.5	224	1.29	11.8	< 13.55	COS-GASS
J1544+2740_28317	0.0320	0.163	< -12.1	10.1	196	1.49	11.4	< 12.72	COS-GASS
J0226+0015_268_22	0.2274	0.615	< -11.8	10.8	80	0.32	12.3	< 13.13	COS-Halos
J0401-0540_67_24	0.2197	0.570	-10.1	10.1	83	0.60	11.6	> 14.26	COS-Halos
J0950+4831_177_27	0.2119	0.589	< -11.7	11.2	92	0.16	13.4	> 14.22	COS-Halos
J1016+4706_274_6	0.2520	0.822	-10.4	10.2	23	0.16	11.6	> 14.48	COS-Halos
J1016+4706_359_16	0.1661	0.822	-10.4	10.5	44	0.26	11.8	> 14.66	COS-Halos
J1342-0053_157_10	0.2270	0.326	-10.2	10.9	35	0.11	12.8	< 13.71	COS-Halos
J1342-0053_77_10	0.2013	0.326	< -11.0	10.5	32	0.19	11.8	< 12.87	COS-Halos
J1419+4207_132_30	0.1792	0.873	-9.5	10.6	88	0.46	11.9	> 14.52	COS-Halos

**Note.** Comments on columns. Column (1): galaxy name: for the COS-Halos galaxies, the value is the SDSS field identifier and galaxy identifier, where the first number is the position angle in degrees from the QSO and the second number is the projected separation in arcseconds (impact parameter) from the QSO; for the COS-GASS, the value is the COS-GASS ID. Column (2): galaxy redshift; column (3): QSO redshift; column (4): specific star formation rate (sSFR). For more details on how the sSFRs were calculated for the galaxies in the sample, refer to J. K. Werk et al. (2012), R. Bordoloi et al. (2014), S. Borthakur et al. (2015), and S. L. Garza et al. (2024). On average, for galaxies of these masses, sSFR errors will be on the order of a few to several tenths of a dex. Column (5): stellar mass: stellar masses are accurate to about  $\sim 50\%$ ; column (6): impact parameter; column (7): impact parameter normalized by virial radius; column (8): virial halo mass; column (9): C IV column density; column (10): which survey the galaxy was matched to, either COS-Halos (J. K. Werk et al. 2013) or COS-GASS (S. Borthakur et al. 2015).

COS-GASS (S. Borthakur et al. 2015). For this reason, we initiated the C IV in  $L^*$  galaxies (CIViL\*) survey to fill this notable gap in previous COS absorption galaxy studies by providing near-ultraviolet coverage of C IV for galaxies with existing O VI measurements in the CGM. For this work, we assume a flat-universe  $\Lambda$ CDM cosmology with  $H_0 = 67.8 \text{ km s}^{-1} \text{ Mpc}^{-1}$  and  $\Omega_m = 0.308$  (Planck Collaboration et al. 2016).

## 2. Observation and Data Analysis

### 2.1. Sample Selection

The CIViL\* survey (PID#17076) more than doubles the number of literature sight lines that probe C IV in the inner CGM of  $L^*$  galaxies. It consists of nine UV-bright QSOs, probing the halos of eleven low-redshift ( $z \lesssim 0.25$ ) galaxies. One of the main goals of this survey is to observe C IV in galaxies that have published O VI detections. To build the survey, we identified galaxies from COS-Halos (J. K. Werk et al. 2013) and COS-GASS (S. Borthakur et al. 2015) that would provide a valuable legacy data set of C IV coverage within one virial radius. This sample of 11 galaxies is representative of the broad range in galaxy stellar mass ( $\log_{10} M_*/M_{\odot} \sim 10.1\text{--}11.4$ ) and impact parameter ( $R_{\text{proj}} \sim 20\text{--}224 \text{ kpc}$ ) of the  $L^*$  galaxies observed in previous COS-CGM programs (e.g., J. K. Werk et al. 2013; R. Bordoloi et al. 2014; S. Borthakur et al. 2015; T. Heckman et al. 2017; T. A. M. Berg et al. 2018; S. L. Garza et al. 2024) in order to enable fair comparisons to other galaxy types in different stages of evolution.

In particular, the final sample was selected by maximizing the number of  $\sim L^*$  galaxies that are simultaneously control matched in both  $M_*$  and  $R_{\text{proj}}$  within  $\pm 0.2$  dex (see T. A. M. Berg et al. 2018 for more details) to previous COS-CGM programs that include a variety of special evolutionary phases of galaxies (i.e., starburst or AGN). Furthermore, the ratio of impact parameter to virial radius of the survey is well matched (within  $\pm 0.3$  dex) to the distribution in the COS-Dwarfs (R. Bordoloi et al. 2014) survey, which enables a similar comparison of radial profiles over the two decades of galaxy mass in a systemic fashion with C IV. At least

three “normal” galaxies were control matched to the starburst or AGN galaxies, while at least five were matched to COS-Dwarf galaxies. Work utilizing this controlled match aspect of the sample to uncover the nature of highly ionized gas surrounding AGN hosts is forthcoming in T. A. M. Berg et al. (2024, in preparation). The focus of this paper is the comparison between passive and star-forming  $\sim L^*$  galaxies.

To create an average profile, normalized by the virial radius, we need the virial radii and virial masses. To estimate dark matter halo masses, we use the same methodology as K. Tchernyshyov et al. (2022). We use the stellar mass–halo relation defined in P. Behroozi et al. (2019, see Table J1 for fit parameters) in combination with the technique described in W. Hu & A. V. Kravtsov (2003). This technique converts the calculated halo masses, estimated using the galaxy stellar mass and redshift, such that the average mass density within the halo radius is 200 times the critical density of the Universe. Using our newly converted virial halo masses ( $M_{200c}$ ), we calculate virial radii ( $R_{200c}$ ). These and other galaxy properties can be found in Table 1.

### 2.2. COS Spectroscopy

The quasar spectra for the CIViL\* survey were taken using either the G160M or the G185M grating on the COS (C. S. Froning & J. C. Green 2009; J. C. Green et al. 2012) on the HST as a part of a 52-orbit Cycle 29 HST Program (PID#17076). The primary spectral features of interest are absorption lines from the C IV doublet ( $\lambda\lambda 1548, 1550$ ) at the redshift of each host galaxy. The CIViL\* QSOs have far-ultraviolet magnitudes of  $\sim 17.0\text{--}18.4$  and redshifts ranging from 0.032 to 0.252. Each target QSO was observed between 2–5 orbits in either G185M (targets matched to COS-Halos; J. K. Werk et al. 2013) or G160M (targets matched to COS-GASS; S. Borthakur et al. 2015), depending on the galaxy redshift. Our exposure times were calculated to detect a 50 mÅ feature at a confidence of  $2\sigma$ . The signal-to-noise ratio of the resultant spectra range from 5–12 per resel at the wavelengths of the C IV doublet.

We combine the CALCOS-generated x1D files using v3.1.1 of the COADD\_X1D routine provided by the COS-GTO team (C. W. Danforth et al. 2016), which properly treats the error arrays of the input files using Poisson statistics. The IDL COADD\_X1D routine was modified to ingest new data from the G185M grating. The code aligns the different exposures by determining a constant offset determined by cross-correlating strong interstellar medium (ISM) lines in a 10 Å wide region of the spectrum. For data taken with the G160M grating, each COS resolution element at  $R \sim 18,000$  is sampled by six raw pixels at 12.23 mÅ per pixel. G185M spectra consist of three 35 Å stripes separated by two 64 Å gaps with an  $R \sim 18,000$  and typical spectral dispersion of 33 mÅ per pixel (0.2 Å per 6 pixel resolution element). Both the G160M and G185M spectra are Nyquist sampled. For G160M, we binned to Nyquist sampling with two bins per resolution element. The spectra for G185M, which are slightly lower resolution, are well sampled and did not require binning. The resulting science-grade spectra are characterized by an FWHM  $\approx 16 \text{ km s}^{-1}$  and  $\approx 38 \text{ km s}^{-1}$  for G160M and G185M data, respectively. We perform continuum fitting with the `linetools` package,<sup>6</sup> an open-source code for analysis of 1D spectra.

### 2.3. Absorption Line Measurements

We determine absorption feature line identifications and redshifts in the CIViL\* spectra using the PyIGM IGMGuesses graphical user interface (GUI).<sup>7</sup> Since the redshifts of the galaxies in the CIViL\* survey are well known (see Table 1) CGM absorption features were identified by scanning the spectra for features within  $\sim 300 \text{ km s}^{-1}$  associated with the C IV doublet ( $\lambda\lambda 1548, 1550$ ). If blends or absorption other than C IV were present, we followed the same identification methodology described in S. L. Garza et al. (2024).

Based on the manual identifications from the PyIGM IGMGuesses GUI, we measure the C IV column densities ( $N_{\text{C IV}}$ ), Doppler parameter ( $b$ ), and the relative velocity of the absorption components ( $v_{\text{rel}}$ ) using the Voigt profile fitting with the package `veeper`.<sup>8</sup> This package uses `scipy.optimize.least_squares`<sup>9</sup> to perform a least-squares minimization to obtain its measurements and incorporates the COS line spread function. Five of our QSO–galaxy line-of-sight pairs show C IV detections (Figure 1); however, the absorption features are saturated, so we report them as lower limits. When multiple absorption components are found in a galaxy's search window, their column densities are summed, and the resulting total column density is associated with the galaxy. The other five of the line-of-sight pairs show no C IV absorption, and we report them as upper limits. In these nondetection regions, we calculate a  $2\sigma$  upper limit on the column density as estimated by the apparent optical depth method with the `linetools XSpectrum1D` package<sup>10</sup> over a  $100 \text{ km s}^{-1}$  velocity span centered on the galaxy redshift. By default, we use the stronger line at 1548 Å to estimate  $2\sigma$  equivalent width upper limits, but in cases where there is blending or contamination, we use the 1550 Å line. Our C IV column density measurements can be found in Table 1, and they are shown as a function of the

impact parameter normalized by virial radius and stellar mass in panels 2 and 3 of Figure 2, respectively.

### 2.4. Archival Observations

Previous studies have shown that observable tracers of the CGM depend on galaxy mass, redshift, and environment (J. Bergeron 1986; J. N. Bahcall et al. 1991; H.-W. Chen et al. 2001; J. T. Stocke et al. 2006; R. Bordoloi et al. 2011; J. K. Werk et al. 2013; S. D. Johnson et al. 2015; J. N. Burchett et al. 2016; N. Tejos et al. 2016; R. Bordoloi et al. 2018; K. Tchernyshyov et al. 2023), making them important variables to consider when studying the differences between the CGM of star-forming and passive galaxies. To address the effect of these galaxy properties, we increase our sample size with CGM C IV measurements using published HST/COS data from COS-Halos (J. K. Werk et al. 2013), COS-Dwarfs (R. Bordoloi et al. 2014), and COS-Holes (S. L. Garza et al. 2024). Eight out of eleven of our QSO–galaxy line-of-sight pairs are COS-Halos (J. K. Werk et al. 2013) galaxies; thus it is intuitive to include the two galaxies from the COS-Halos survey that already have C IV observations. The COS-Holes Survey<sup>11</sup> (S. L. Garza et al. 2024) sits well within the stellar mass and impact parameter range of the CIViL\* survey and adds nine observations to the sample. We also include observations from the COS-Dwarfs survey (R. Bordoloi et al. 2014) because, as mentioned in Section 2.1, the CIViL\* survey is well matched with this survey's ratio of impact parameter to virial radius. By including observations from these three surveys, we have a total combined C IV sample of 65 observations.

## 3. Results

In the top panel of Figure 2, we show the C IV detection fractions ( $C_f$ ), with  $2\sigma$  Wilson binomial confidence intervals<sup>12</sup> for eight equal-sized radial bins. Our detection fractions show that as the normalized impact parameter increases, and the detection fraction of C IV decreases; this declining profile, a trend described in several previous works (e.g., R. Bordoloi et al. 2014), is mirrored in the middle panel.<sup>13</sup> In the middle and bottom panels of Figure 2, we show the C IV column densities versus impact parameter normalized by virial radius or  $R_{\text{proj}}/R_{200c}$  (middle panel) and stellar mass,  $\log_{10}M_*/M_\odot$  (bottom panel), colored by specific star formation rate (sSFR;  $\log_{10}\text{sSFR}/\text{yr}^{-1}$ ).

Given the variation of CGM columns with galaxy mass and redshift found in previous studies (K. Tchernyshyov et al. 2023), for the rest of our analysis, we restrict the sample to  $\log_{10}M_*/M_\odot \geq 9.5$  since below this limit, the vast majority of galaxies are star forming. Additionally, stellar masses lower than this cutoff are mostly dwarf galaxies, where it has been shown that their CGM contains  $\sim 10\%$  of metals in the cool phase ( $T \approx 10^4 \text{ K}$ ; Y. Zheng et al. 2024). This is consistent with what we see in our lower-mass sample, where most of the observations of C IV are upper limits. Introducing this cut leaves us with a sample of 46 observations of galaxies with

<sup>6</sup> <https://github.com/linetools>

<sup>7</sup> <https://github.com/pyigm>

<sup>8</sup> <https://github.com/jnburchett/veeper>

<sup>9</sup> <https://github.com/scipy/scipy>

<sup>10</sup> <https://github.com/linetools/linetools/tree/v0.3>

<sup>11</sup> We note that results from S. L. Garza et al. (2024) suggest that C IV absorption does not show obvious variation as a function of SMBH mass.

<sup>12</sup> This method of calculating confidence intervals is better than normal approximations since it is asymmetric and can be used with small samples and skewed observations.

<sup>13</sup> In Appendix A, we examine other binning methods and find these also result in a covering fraction that declines with the impact parameter.



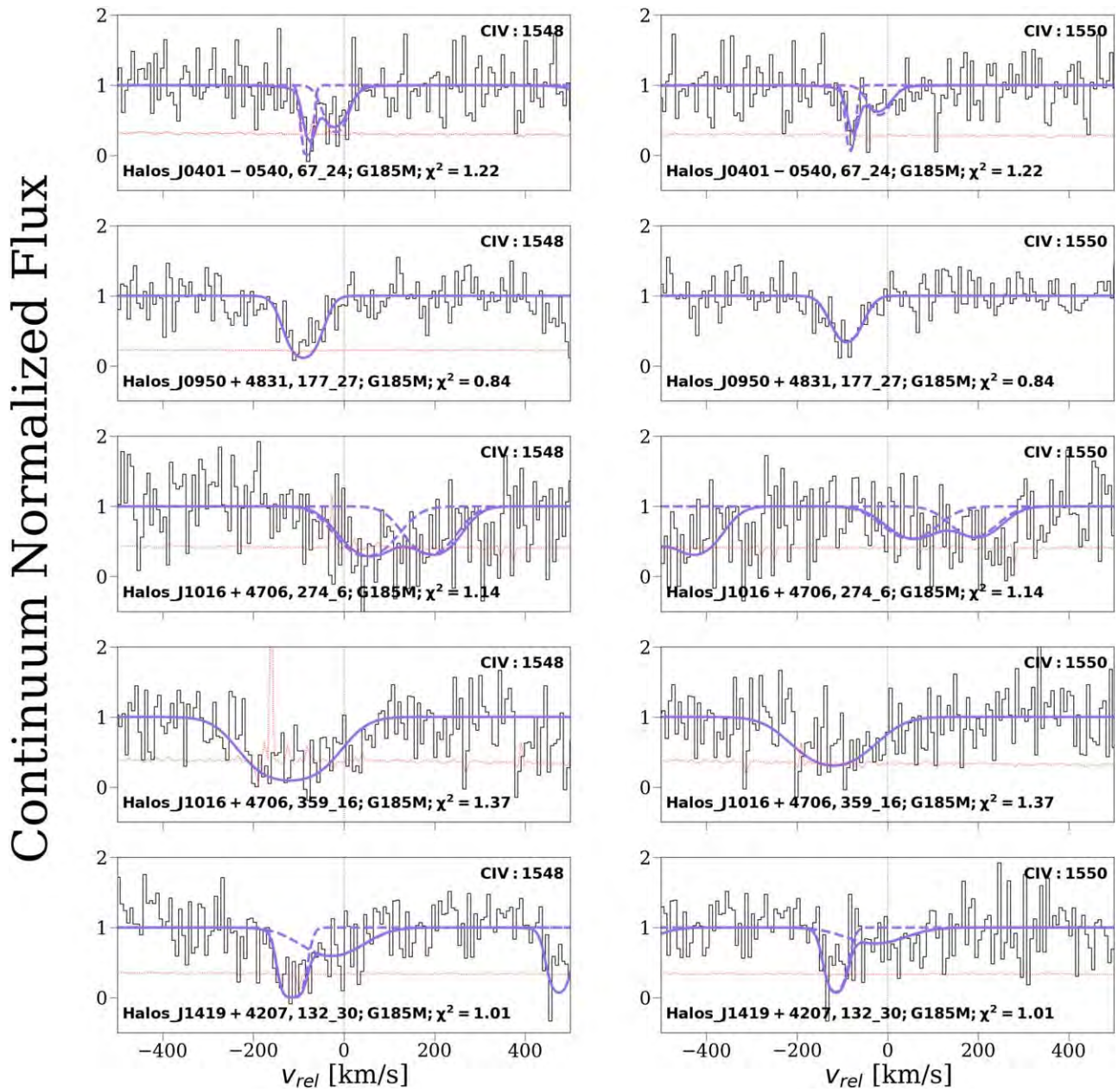


**Figure 1.** Regions of the HST/COS continuum spectrum showing the C IV  $\lambda\lambda$  1548 1550 line absorption features of the CIVL\* QSO–galaxy pairs set in the rest frame of each individual galaxy. For lines of sight that have multiple components, the individual fits are shown as the dashed purple line where the sum of the components is shown as the solid purple line. The red line in each spectrum represents the continuum flux error. The bottom left corner has the QSO–galaxy IDs and the reduced  $\chi^2$  fit for the absorption features.

redshifts between 0.0010 and 0.252, impact parameters of 14–224 kpc, and stellar masses between  $10^{9.5}$  and  $10^{11.2} M_{\odot}$ .

### 3.1. CIV–sSFR Dichotomy

We now examine the relation between CIV and sSFR to investigate whether a similar bimodality exists like the one using O VI (G. Kauffmann et al. 2003; D. Schiminovich et al. 2007; J. Tumlinson et al. 2011; K. Tcheryshyov et al. 2023). We plot  $\log_{10} N_{C\text{IV}}/\text{cm}^{-2}$  versus  $\log_{10} \text{sSFR}/\text{yr}^{-1}$  for the combined small sample in Figure 3. We separate the observations into two galaxy groups based on cuts made in previous works (J. Tumlinson et al. 2011; K. Tcheryshyov et al. 2023), divided into star-forming galaxies ( $\text{sSFR} > 10^{-11} \text{yr}^{-1}$ , blue) and passive galaxies ( $\text{sSFR} \leq 10^{-11} \text{yr}^{-1}$ , red). We paid special attention to galaxies

within  $\pm 0.2$  dex of this cutoff, represented as the gray shaded area in Figure 3. Galaxies in this area are possibly transitioning between star forming and passive and have subtleties that define their classification that a simple sSFR cut does not catch. For the galaxies that fall within this “gray” area, we referred to their optical spectra and morphology to determine their classification; for more details, we refer the reader to Appendix B.

We find detection fractions of  $72_{-18}^{+14}\%$  [21/29] for the star-forming sample and  $23_{-15}^{+27}\%$  [3/13] for the passive sample with  $2\sigma$  Wilson binomial confidence intervals above  $\log_{10} N_{C\text{IV}}/\text{cm}^{-2} = 13.5$ .<sup>14</sup> Using `scipy.stats.anderson_ksamp`,<sup>15</sup> we perform an

<sup>14</sup> See Appendix C for an exploration of detection fractions using different detection thresholds

<sup>15</sup> <https://github.com/scipy/scipy>

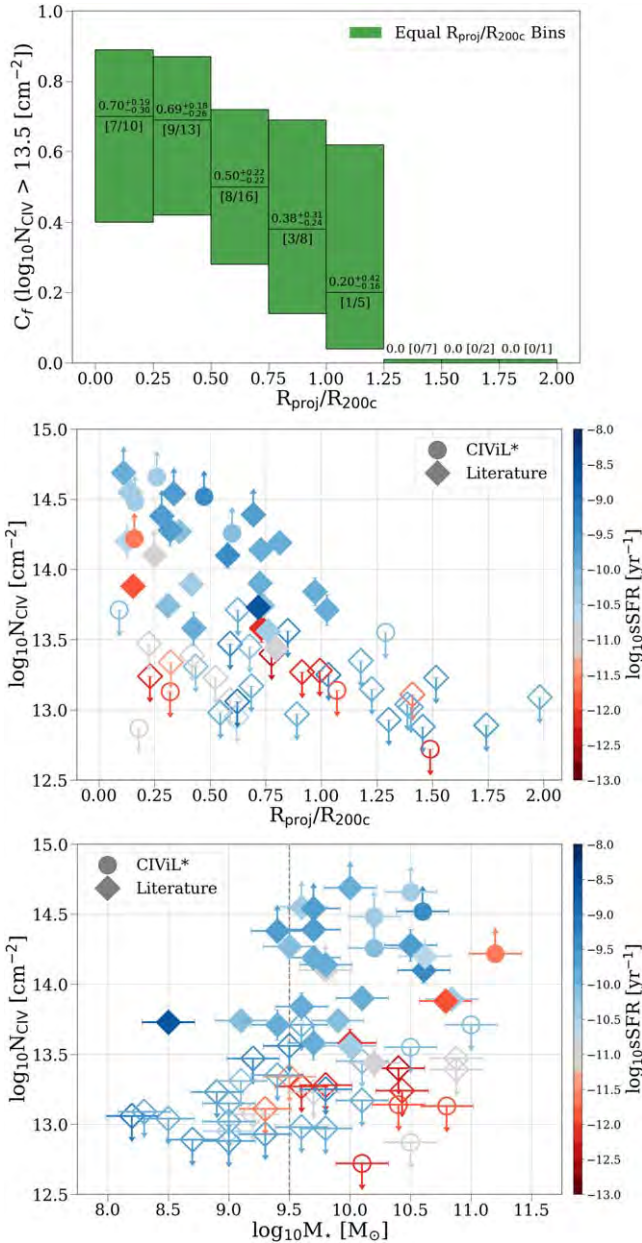


**Figure 2.** Top panel: the CIV detection fraction vs. normalized impact parameter. The shaded areas represent  $2\sigma$  Wilson binomial confidence intervals across equal-width radial bins. Upper limits exceeding the threshold ( $\log_{10} N_{\text{CIV}}/\text{cm}^{-2} = 13.5$ ) are excluded from the analysis. Middle and bottom panels: CIV column densities assembled from previous QSO absorption line surveys probing the CGM of low- $z$  galaxies (diamonds) with the new CIVIL\* observations (circles) vs. galaxy properties (middle:  $R_{\text{proj}}/R_{200c}$ ; bottom:  $\log_{10} M_*/M_\odot$ ). Each observation is colored by its corresponding sSFR determined from a combination of emission-line spectroscopy and broadband photometry. Nondetections (upper limits) are represented with open symbols and arrows pointing down, while saturated detections (lower limits) are represented as filled symbols with arrows pointing up. For the rest of the analysis, we only use observations with a  $\log_{10} M_*/M_\odot \geq 9.5$ .

Anderson–Darling test for  $k$ -samples<sup>16</sup> to compare the CIV column densities of the star-forming (33) and passive (13) samples. For this test, we treat each observation as if it were a

<sup>16</sup> The  $k$ -sample Anderson–Darling test is a modification of the one-sample Anderson–Darling test. It tests the null hypothesis that  $k$ -samples are drawn from the same population without having to specify the distribution of that population.

detection (i.e., not taking into account upper and lower limits); the Anderson–Darling test is useful when not taking into account known limits since the test is designed to examine the tails of distributions, which makes it particularly sensitive to deviations in extreme values. We find that we can reject the null hypothesis that these two samples were drawn from the same distribution at a  $>99.5\%$  confidence level ( $p = 0.0016$ ). We also explore statistical methods that take into account censored data (upper and lower limits) in Appendix D; both of these alternative methods (interval-censored analysis:  $p = 0.017$ , two-sided  $k$ -sample test:  $p = 0.034$ ) confirm our original finding that there is a bimodality between the CIV content in star-forming and passive galaxies with  $>2\sigma$  confidence.

We also test the statistical significance of the correlation of  $N_{\text{CIV}}$  and sSFR by performing a generalized Kendall’s tau test using `scipy.stats.kendalltau`.<sup>17</sup> This test, which did not take into account upper or lower limits, resulted in a  $\tau = 0.29$  ( $p = 0.004$ ), which leads us to reject the null hypothesis that there is no correlation between the CIV absorption and galaxy sSFR. R. Bordoloi et al. (2014) report a similar result for galaxies with  $9 \leq \log_{10} M_*/M_\odot \leq 10$ , where they also rejected the null hypothesis that star-forming and passive galaxies draw from the same parent distribution of equivalent widths at a  $>99.5\%$  confidence level. Similar Kendall’s tau tests using O VI column densities were performed by J. Tumlinson et al. (2011), where they used QSO–galaxy pairs from the COS-Halos survey (J. K. Werk et al. 2013). They also found that  $N_{\text{O VI}}$  and sSFR correlate at a  $>99\%$  confidence, which led them to conclude that their results show a basic dichotomy between star-forming (“blue cloud”) and passive (“red sequence”) galaxies is present in the gaseous halos of their sample.

To compare between our result and the O VI–sSFR dichotomy, we recreate Figure 3 from J. Tumlinson et al. (2011), as seen in Figure 4. We highlight galaxies in which CIV and O VI were both observed in dark, bold points. These observations overlay the lightly shaded O VI column densities from J. Tumlinson et al. (2011) and J. K. Werk et al. (2013) and CIV observations from the combined CIVIL\* and literature sample. Our results independently suggest a dichotomy between the halos of star-forming and passive galaxies as traced by CIV but overlaid with O VI; they statistically mirror the dichotomy discussed in J. Tumlinson et al. (2011).

### 3.2. Minimum Mass of Carbon in the CGM

We estimate the total mass of carbon in the CGM  $\sim L^*$  galaxies by following the method outlined in R. Bordoloi et al. (2014). By assuming a conservative ionization correction ( $f_{\text{CIV}} = 0.3$ ; for more details, please see Section 5 in R. Bordoloi et al. 2014), they obtained a lower limit on the carbon mass ( $M_{\text{carbon}}$ ), which can be written as

$$M_{\text{carbon}} \gtrsim 1.12 \times 10^6 M_\odot \left( \frac{N_{\text{CIV,mean}}}{10^{14} \text{ cm}^{-2}} \right) \times \left( \frac{R_{\text{proj}}}{120 \text{ kpc}} \right)^2 \times \left( \frac{0.3}{f_{\text{CIV}}} \right). \quad (1)$$

Similarly to R. Bordoloi et al. (2014), we split our sample into three radial bins and then summed them to obtain the final lower limit on carbon mass. The mean column density within

<sup>17</sup> <https://github.com/scipy/scipy>



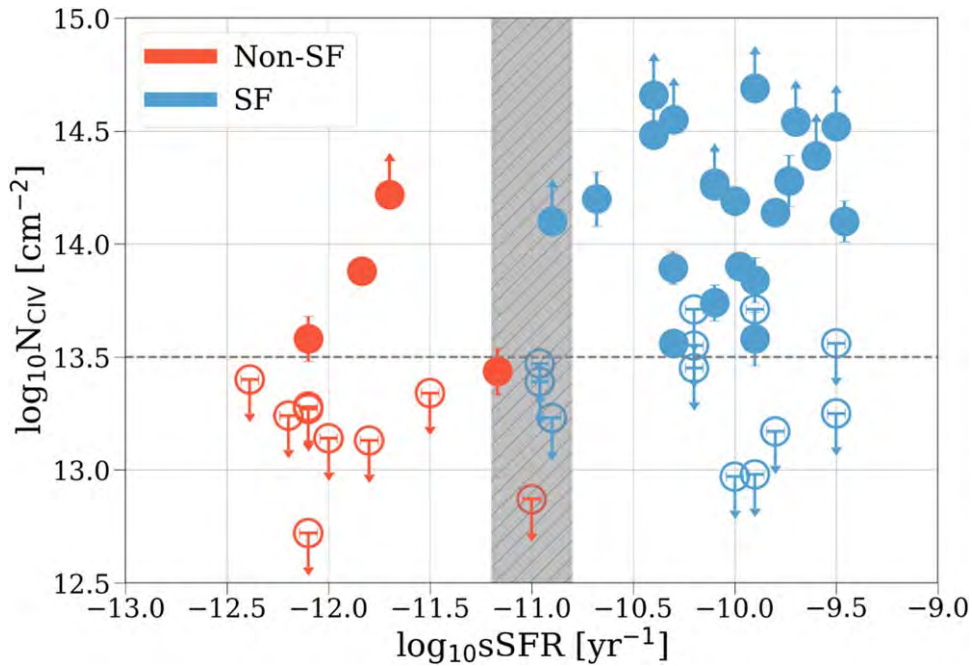


**Figure 3.** Measured C IV column densities vs. sSFR for CIViL\* and the additional literature sample, with star-forming galaxies (sSFR  $> 10^{-11} \text{ yr}^{-1}$ ) colored in blue, while passive galaxies (sSFR  $\leq 10^{-11} \text{ yr}^{-1}$ ) are colored in red. For galaxies in the gray shaded area, we examine their spectra and morphology, in addition to sSFR for classification. Like the previous figure, nondetections (upper limits) are represented with open symbols and arrows pointing down, while saturated detections (lower limits) are represented as filled symbols with arrows pointing up. The horizontal line signifies the detection limit of the sample. Above  $\log_{10} N_{\text{C IV}}/\text{cm}^{-2} = 13.5$ , the star-forming and passive galaxy sample have detection fractions of  $72^{+14}_{-18}\%$  [21/29] and  $23^{+27}_{-13}\%$  [3/13], respectively. Upper limits exceeding the threshold are excluded from the analysis.

$R_{\text{proj}} < 40 \text{ kpc}$  is  $2.10 \times 10^{14} \text{ cm}^{-2}$ , within  $40 \text{ kpc} \leq R_{\text{proj}} < 80 \text{ kpc}$  is  $1.44 \times 10^{14} \text{ cm}^{-2}$ , and within  $80 \text{ kpc} \leq R_{\text{proj}} < 120 \text{ kpc}$  is  $1.65 \times 10^{14} \text{ cm}^{-2}$ .

We find a minimum carbon mass of  $M_{\text{carbon}}/M_{\odot} \gtrsim 3.03 \times 10^6$ . We note that the column densities derived using Voigt profile fits are saturated for some of the lines of sight in the sample and are thus probably underestimating the true column density; however, this value is about a factor of 1.6 higher than the  $M_{\text{carbon}}$  value presented in R. Bordoloi et al. (2014) ( $1.9 \times 10^6 M_{\odot}$ ). Our minimum carbon mass is comparable to the total carbon mass in the ISM of L\* galaxies (e.g., M. S. Peebles et al. 2014; R. Bordoloi et al. 2014).

#### 4. Discussion

Results from the COS-Dwarfs survey (R. Bordoloi et al. 2014) suggested a correlation between C IV absorption strength and sSFR of sub-L\* galaxies within half the virial radius. The COS-Holes survey (S. L. Garza et al. 2024) tentatively confirmed with  $\gtrsim 2\sigma$  significance that a correlation between sSFR and C IV-bearing CGM in L\* galaxies is similar to that of O VI. The combined CIViL\* observations with those from other COS-CGM surveys indicate that C IV is more O VI-like than “low-ion-like.” This suggests that C IV is also tracing gas formed or maintained by star formation and/or feedback unlike other low-ionization state gas traced by singly and doubly ionized species (e.g., HI, Si II, C III, etc) which show no correlation with galaxy star-forming properties (J. K. Werk et al. 2013). In an upcoming paper, we will perform a detailed analysis of the kinematics and ionization state of C IV-bearing gas to provide more complete constraints on the physical conditions of the CGM of  $\sim L^*$  galaxies.

CGM C IV also provides a potential avenue for exploring how galaxies sustain their star formation since the CGM is a large gaseous reservoir and a source for the galaxy’s star-forming fuel (J. Tumlinson et al. 2017). To address this, we estimate the depletion time,  $\tau_{\text{dep}}$ , as the CGM mass divided by the mean star formation rate (SFR), the timescale over which star formation could be maintained its current rate, given an available gas supply, and assuming no inflows of fresh fuel or recycling of the gas (A. Saintonge & B. Catinella 2022). But how much fuel is actually available? To do this back-of-the-envelope calculation, we use the minimum mass of carbon we estimate in Section 3.2 (for a conservative ionization correction) and translate it to a total hydrogen mass using a metallicity of  $Z = 1/3$  (J. X. Prochaska et al. 2017) and the solar carbon abundance. This gives a lower limit of  $M_{\text{CGM}} \geq 2.83 \times 10^9 M_{\odot}$  on the total gas mass in the CGM. Using the mean SFR in our sample,  $1.5 M_{\odot} \text{ yr}^{-1}$ , the resulting lower limit on the depletion time is  $\tau_{\text{dep}} \geq 1.93 \text{ Gyr}$ .

Comparing our depletion time to depletion times presented in Figure 6(a) of C. Péroux & J. C. Howk (2020), we find that our  $\tau_{\text{dep}}$  is fairly consistent with their molecular gas depletion timescale at  $z = 0$ . Our depletion timescale is comparable or shorter than the dynamical timescale (taken to be 10% of the Hubble time) which suggests that the CGM and molecular gas available to galaxies, assuming no inflows of fresh fuel or recycling of the gas, slowly becomes insufficient to fuel star formation on its own (C. Péroux & J. C. Howk 2020). Therefore, galaxies are most likely undergoing some resupply process either through the conversion of ionized gas from the CGM or IGM or through accretion from the IGM onto the disks of galaxies. Thus, gas in the CGM is only one piece of the large reservoir that galaxies use as fuel for future star formation.

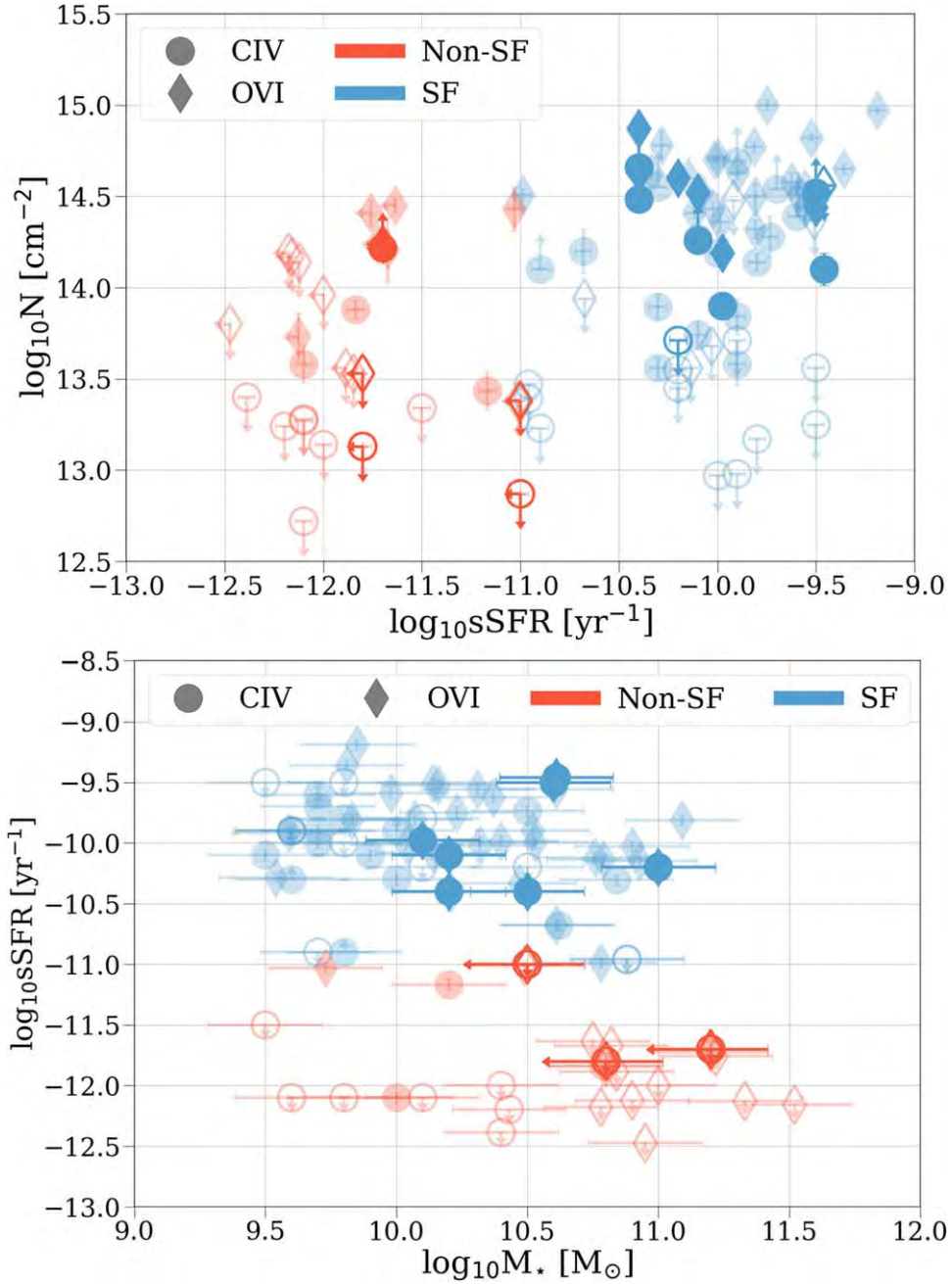


**Figure 4.** C IV and O VI correlations with galaxy properties. If the marker is dark/bold, they are from galaxies where both ions were observed. These observations overlay lightly shaded O VI column densities from J. Tumlinson et al. (2011) and J. K. Werk et al. (2013) and C IV observations from the combined CIViL\* and literature sample. Similar coloring and limit convention as Figure 3. Top:  $\log_{10}N_{\text{C IV}}/\text{cm}^{-2}$  and  $\log_{10}N_{\text{O VI}}/\text{cm}^{-2}$  vs.  $\log_{10}\text{sSFR}/\text{yr}^{-1}$ . Bottom:  $\log_{10}N_{\text{C IV}}/\text{cm}^{-2}$  and  $\log_{10}N_{\text{O VI}}/\text{cm}^{-2}$  vs.  $\log_{10}M_*M_{\odot}$ . The basic dichotomy observed between star-forming (“blue cloud”) and passive (“red sequence”) galaxies seen in O VI observations (J. Tumlinson et al. 2011; S. D. Johnson et al. 2015; F. S. Zahedy et al. 2019; K. Tchennyshyov et al. 2023) is also seen in observations of C IV.

## 5. Summary and Conclusion

In this work, we presented observations from the CIViL\* survey. The main results of this study are as follows.

1. The CIViL\* Survey amplifies the diagnostic power of the current COS-CGM samples through the acquisition of 11 new C IV observations for  $L^*$  galaxies.
2. We combine our observations from CIViL\* with C IV observations (J. K. Werk et al. 2013; R. Bordoloi et al. 2014; S. L. Garza et al. 2024) for a final sample of 45

lines of sight. We separate the observations by their sSFR, where we classify them as either star forming ( $\text{sSFR} > 10^{-11} \text{ yr}^{-1}$ ) or passive ( $\text{sSFR} \leq 10^{-11} \text{ yr}^{-1}$ ).

3. We find a detection fraction of  $72_{-18}^{+14}\%$  [21/29] for the star-forming sample and  $23_{-15}^{+27}\%$  [3/13] for the passive sample. Using an Anderson–Darling test to compare C IV absorption in star-forming and passive galaxies, we find a dichotomy at a  $>99.5\%$  confidence level.
4. Our discovery of a dichotomy in  $L^*$  galaxies is similar to the one found using O VI-bearing gas (J. Tumlinson et al. 2011; K. Tchennyshyov et al. 2023).

The results from this paper are the tip of the iceberg for what observations from the CIVIL<sup>\*</sup> survey will reveal. This survey supplements the enormous investment of 483 orbits in previous COS-CGM surveys by placing one of the most consistent ion tracers of diffuse gas in the context of the baryon cycle over 10+ Gyr of cosmic evolution. Not only does it close a gap in CIV coverage for low-*z*, L<sup>\*</sup> galaxies, it also provides the opportunity to constrain how the baryon cycle differs among dwarf, star-forming, passive, and AGN-bearing galaxies. Future work carried out using the CIVIL<sup>\*</sup> survey data will examine the kinematics and ionization mechanisms of the CIV-traced gas phase of the CGM and the differences between the CGM of AGN hosts and star-forming galaxies.

### Acknowledgments

Based on observations with the NASA/ESA Hubble Space Telescope through program number HST-GO-17076, obtained at the Space Telescope Science Institute, which is operated by the Association of Universities for Research in Astronomy, Incorporated, under NASA contract NAS5-26555. Additional data comes from HST-GO programs: COS-Halos PID#11598, COS-Dwarfs PID#12248, COS-Holes PID#16650. This research has made use of the NASA/IPAC Extragalactic Database (NED), which is operated by the Jet Propulsion Laboratory, California Institute of Technology, under contract with the National Aeronautics and Space Administration.

We thank the anonymous referee for insightful comments that improved the quality of the paper. S.L.G. recognizes the unceded traditional lands of the Duwamish and Puget Sound Salish Tribes, where she is grateful to love and work. They also thank Boeun Choi and Kirill Tchernyshyov for enlightening conversations and advice that helped improve this work. Y.F. acknowledges support by NASA award 19-ATP19-0023 and NSF award AST-2007012.

*Facility:* HST(COS).

*Software:* astropy (Astropy Collaboration et al. 2013, 2018), Cloudy (G. J. Ferland et al. 2013), interval (M. P. Fay & P. A. Shaw 2010), linetools (J. X. Prochaska et al. 2017a), matplotlib (J. D. Hunter 2007), numpy (C. R. Harris et al. 2020), pandas (pandas development team 2024), PyIGM (J. X. Prochaska et al. 2017b), scipy (P. Virtanen et al. 2020), veeper (J. Burchett 2024).

### Data Availability

HST/COS spectra can be found in MAST doi:[10.17909/dgjk-f804](https://doi.org/10.17909/dgjk-f804).

## Appendix A Full Sample Detection Fractions

In addition to calculating covering fractions for equal radial bins, we created radial bins that had an equal amount of galaxies per bin. We list detection fractions from both of these scenarios in Table A1. Again, our detection fractions reflect the declining radial profile seen in the middle panel of Figure 2.

**Table A1**  
Full Sample Detection Fractions

Bin Width (1)	Hit Rate (2)	$C_f$ (3)	$2\sigma$ CI (4)
Four Equal Radial Bins ( $R_{\text{proj}}/R_{200c}$ )			
0.0–0.5	16/23	0.70	(0.49, 0.84)
0.5–1.0	11/24	0.46	(0.28, 0.65)
1.0–1.5	1/11	0.09	(0.02, 0.38)
1.5–2.0	0/3	0.00	(0, 0)
Eight Equal Radial Bins ( $R_{\text{proj}}/R_{200c}$ )			
0.0–0.25	7/10	0.70	(0.40, 0.89)
0.25–0.5	9/13	0.69	(0.42, 0.87)
0.5–0.75	8/16	0.50	(0.28, 0.72)
0.75–1.0	3/8	0.38	(0.14, 0.69)
1.0–1.25	1/5	0.20	(0.04, 0.62)
1.25–1.5	0/7	0.00	(0, 0)
1.5–1.75	0/2	0.00	(0, 0)
1.75–1.0	0/1	0.00	(0, 0)
Equal Number of Galaxies per Bin ( $R_{\text{proj}}/R_{200c}$ )			
0.1–0.3	9/12	0.75	(0.47, 0.91)
0.3–0.5	7/13	0.54	(0.29, 0.77)
0.6–0.7	6/12	0.50	(0.25, 0.75)
0.7–1.0	6/12	0.50	(0.25, 0.75)
1.0–2.0	0/12	0.00	(0, 0)

**Note.** Comments on columns. Column (1): width of the radial bins; column (2): hit rate—the amount of detections above the threshold of  $\log_{10}N_{\text{CIV}}/\text{cm}^{-2} = 13.5$ ; column (3): detection fractions; column (4):  $2\sigma$  Wilson binomial confidence intervals.

## Appendix B Galaxies in the “Gray” Area

There are five galaxies in our sample that have sSFRs that fall within a “gray” area of  $\pm 0.2$  dex around our cutoff of  $\log_{10}\text{sSFR}/\text{yr}^{-1} = -11.0$ , or the area where galaxies are transitioning between star forming and passive. To classify these galaxies as either star forming or passive, we took extra steps in addition to looking at their sSFR. Our explanation for our choice to denote a galaxy as either star forming or passive is detailed below:

1. *SDSS J110404.25+314015.1 (COS-Dwarfs, 211\_65, R. Bordoloi et al. 2014).* We looked at the spectrum available through the Sloan Digital Sky Survey (SDSS) and observed strong emission lines indicative of a late-type galaxy. We group this galaxy in the star-forming bin for our analysis.
2. *SDSS J082022.99+233447.4 (COS-Halos and COS-Dwarfs, 260\_17, J. K. Werk et al. 2013; R. Bordoloi et al. 2014).* We looked at the spectrum available through SDSS and observed both absorption and emission features. We investigated the galaxy’s emission-line ratios and compared them to an SDSS Baldwin, Phillips & Terlevich diagram and saw that it lies within the star-forming region. In addition, this galaxy is a dusty,



edge-on disk galaxy with an  $\log_{10}\text{sSFR}/\text{yr}^{-1} = -10.9$ . Thus, we place this galaxy in the star-forming group for our analysis.

3. *NGC 4258 (COS-Holes, S. L. Garza et al. 2024)*. We looked at the spectrum available on NASA/IPAC Extragalactic Database (NED)<sup>18</sup> and observed strong emission features indicative of a late-type galaxy. We also investigated the morphology of NGC 4258 and found it to be a weakly barred spiral galaxy. Due to these findings, we place this galaxy in the star-forming group for our analysis.
4. *NGC 3489 (COS-Holes, S. L. Garza et al. 2024)*. We looked at the spectrum available on NED and observed both emission and absorption features. Looking at the morphology, we find that the galaxy is an intermediate spiral. Taking into consideration its sSFR ( $\log_{10}\text{sSFR}/\text{yr}^{-1} = -11.167$ ), we group this in the passive galaxy group.
5. *SDSS J134252.23-005343.2 (COS-Halos, 77\_10, J. K. Werk et al. 2013)*. We looked at the spectrum available in J. K. Werk et al. (2012) and determined that it is very clearly an early-type galaxy from the spectrum with distinct absorption lines. We place this galaxy in the passive group for our analysis.

### Appendix C

#### Star-forming and Passive Detection Fractions

Here, we compare the detection fractions calculated using different detection thresholds as shown in Table C1. Upper limits exceeding the threshold are excluded from the analysis, counting as neither detections nor nondetections. The probability distribution for the detection fraction is characterized by a Beta distribution:

$$p(f|k, N) = \text{Beta}(\alpha = k + c, \beta = N - K + c). \quad (\text{C1})$$

The likelihood of observing  $k$  detections in  $N$  trials given a detection probability  $f$  is given by the binomial distribution. The posterior probability distribution for  $f$  given an observed number of detections and assuming a Jeffreys's prior on  $f$  is a beta distribution with parameters  $\alpha = k + 1/2$  and  $\beta = N - k + 1/2$ . This beta distribution arises from the normalization of a binomial probability mass function  $P(k|N, f) \propto f^k(1 - f)^{N-k}$  with respect to the parameter  $f$  rather than the count  $k$ . The statistical comparison of detection fractions is performed through Monte Carlo sampling from the respective beta distributions. For each pair of covering fractions, we examine ratio distributions  $f_{\text{SF}}/f_{\text{P}}$ . The results of these distributional comparisons across detection fraction thresholds are summarized as follows:

1. *Detection Threshold of  $\log_{10}N_{\text{C IV}}/\text{cm}^{-2} = 13.5$* . The analysis indicates that the star-forming detection fraction exceeds the passive detection fraction by a factor of 2–5, measured within the 68% credible interval. The probability of the passive detection fraction surpassing the star-forming detection fraction is  $p = 1.2 \times 10^{-3}$ , corresponding to a  $3\sigma$  deviation under the assumption of normality.

<sup>18</sup> The NED is funded by the National Aeronautics and Space Administration and operated by the California Institute of Technology.

**Table C1**  
SF and Non-SF Detection Fractions

Galaxy Group	Hit Rate	$C_f$ %	$2\sigma$ CI
(1)	(2)	(3)	(4)
Detection Threshold: $\log_{10}N_{\text{C IV}}/\text{cm}^{-2} = 13.5$			
SF	21/29	72	(54, 85)
Non-SF	3/13	23	(8, 50)
Detection Threshold: $\log_{10}N_{\text{C IV}}/\text{cm}^{-2} = 13.75$			
SF	18/33	54	(38, 70)
Non-SF	2/13	15	(4, 42)
Detection Threshold: $\log_{10}N_{\text{C IV}}/\text{cm}^{-2} = 14.0$			
SF	15/33	45	(30, 62)
Non-SF	1/13	8	(1, 33)

**Note.** Comments on columns. Column (1): galaxy group—either star-forming (SF) or passive (non-SF); column (2): hit rate—the amount of detections above the indicated detection threshold; column (3): detection fractions; column (4):  $2\sigma$  Wilson binomial confidence intervals.

2. *Detection Threshold of  $\log_{10}N_{\text{C IV}}/\text{cm}^{-2} = 13.75$* . The analysis indicates that the star-forming detection fraction exceeds the passive detection fraction by a factor of 2–7, measured within the 68% credible interval. The probability of the passive detection fraction surpassing the star-forming detection fraction is  $p = 6.2 \times 10^{-3}$ , corresponding to a  $2.5\sigma$  deviation under the assumption of normality.
3. *Detection Threshold of  $\log_{10}N_{\text{C IV}}/\text{cm}^{-2} = 14.0$* . The analysis indicates that the star-forming detection fraction exceeds the passive detection fraction by a factor of 2–14, measured within the 68% credible interval. The probability of the passive detection fraction surpassing the star-forming detection fraction is  $p = 4.8 \times 10^{-3}$ , corresponding to a  $2.6\sigma$  deviation under the assumption of normality.

### Appendix D





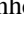


#### Statistical Methods for Censored Data

For observations characterized by detection limits, where measurements are confined by lower and upper bounds, interval-censored statistical methods provide a practical, yet valid, analytical framework. For upper limits, we construct intervals from a common lower bound to the detection threshold, while for lower limits, we construct intervals from the saturation limit to a common upper bound. The implementation of interval-censored survival analysis thus accommodates both left-censored (upper limits) and right-censored (lower limits) data by transforming point constraints into comparable intervals. This approach maintains statistical validity in rank-based tests as the specific values chosen for the common bounds do not affect the relative ordering of the observations, provided these bounds are consistently applied across all measurements and are outside the range of the measurements.

Interval-censored survival analysis was performed using the `interval` package in R to evaluate differences between the survival distributions of the passive and star-forming samples.

The log-rank test with the `logrank1` score function was implemented to test the hypothesis that the survival distribution of the passive sample is stochastically less than that of the star-forming sample. This test yielded statistical significance at  $p = 0.017$ . A subsequent two-sided k-sample test indicated that the survival distributions differ significantly ( $p = 0.034$ ). These interval-censored survival analyses, which explicitly account for the censoring structure in the observations, provide statistical evidence for bimodality in the C IV content between star-forming and passive galaxies at  $>2\sigma$  significance.

### ORCID iDs

Samantha L. Garza  <https://orcid.org/0000-0003-4521-2421>  
 Jessica K. Werk  <https://orcid.org/0000-0002-0355-0134>  
 Trystyn A. M. Berg  <https://orcid.org/0000-0002-2606-5078>  
 Yakov Faerman  <https://orcid.org/0000-0003-3520-6503>  
 Benjamin D. Oppenheimer  <https://orcid.org/0000-0002-3391-2116>  
 Rongmon Bordoloi  <https://orcid.org/0000-0002-3120-7173>  
 Sara L. Ellison  <https://orcid.org/0000-0002-1768-1899>

### References

- Anand, A., Nelson, D., & Kauffmann, G. 2021, *MNRAS*, 504, 65  
 Astropy Collaboration, Price-Whelan, A. M., Sipőcz, B. M., et al. 2018, *AJ*, 156, 123  
 Astropy Collaboration, Robitaille, T. P., Tollerud, E. J., et al. 2013, *A&A*, 558, A33  
 Bahcall, J. N., Jannuzi, B. T., Schneider, D. P., et al. 1991, *ApJL*, 377, L5  
 Behroozi, P., Wechsler, R. H., Hearin, A. P., & Conroy, C. 2019, *MNRAS*, 488, 3143  
 Berg, T. A. M., Ellison, S. L., Tumlinson, J., et al. 2018, *MNRAS*, 478, 3890  
 Bergeron, J. 1986, *A&A*, 155, L8  
 Bordoloi, R., Lilly, S. J., Knobel, C., et al. 2011, *ApJ*, 743, 10  
 Bordoloi, R., Prochaska, J. X., Tumlinson, J., et al. 2018, *ApJ*, 864, 132  
 Bordoloi, R., Tumlinson, J., Werk, J. K., et al. 2014, *ApJ*, 796, 136  
 Borthakur, S., Heckman, T., Tumlinson, J., et al. 2015, *ApJ*, 813, 46  
 Burchett, J. 2024, the Veeper, v1.0, Zenodo, doi:10.5281/zenodo.10993984  
 Burchett, J. N., Tripp, T. M., Bordoloi, R., et al. 2016, *ApJ*, 832, 124  
 Chen, H.-W., Lanzetta, K. M., & Webb, J. K. 2001, *ApJ*, 556, 158  
 Danforth, C. W., Keeney, B. A., Tilton, E. M., et al. 2016, *ApJ*, 817, 111  
 Fay, M. P., & Shaw, P. A. 2010, *J. Stat. Softw.*, 36, 1  
 Ferland, G. J., Porter, R. L., van Hoof, P. A. M., et al. 2013, *RMxAA*, 49, 137  
 Froning, C. S., & Green, J. C. 2009, *Ap&SS*, 320, 181  
 Garza, S. L., Werk, J. K., Oppenheimer, B. D., et al. 2024, *ApJ*, 970, 115  
 Green, J. C., Froning, C. S., Osterman, S., et al. 2012, *ApJ*, 744, 60  
 Harris, C. R., Millman, K. J., van der Walt, S. J., et al. 2020, *Natur*, 585, 357  
 Heckman, T., Borthakur, S., Wild, V., Schiminovich, D., & Bordoloi, R. 2017, *ApJ*, 846, 151  
 Hu, W., & Kravtsov, A. V. 2003, *ApJ*, 584, 702  
 Hunter, J. D. 2007, *CSE*, 9, 90  
 Johnson, S. D., Chen, H.-W., & Mulchaey, J. S. 2015, *MNRAS*, 449, 3263  
 Kauffmann, G., Heckman, T. M., White, S. D. M., et al. 2003, *MNRAS*, 341, 33  
 Kwak, K., & Shelton, R. L. 2010, *ApJ*, 719, 523  
 Lan, T.-W. 2020, *ApJ*, 897, 97  
 Lehner, N., & Howk, J. C. 2011, *Sci*, 334, 955  
 Lehner, N., Wotta, C. B., Howk, J. C., et al. 2018, *ApJ*, 866, 33  
 pandas development team 2024, pandas-dev/pandas: Pandas, v2.2.1, Zenodo, doi:10.5281/zenodo.10697587  
 Peeples, M. S., Werk, J. K., Tumlinson, J., et al. 2014, *ApJ*, 786, 54  
 Péroux, C., & Howk, J. C. 2020, *ARA&A*, 58, 363  
 Planck Collaboration, Ade, P. A. R., Aghanim, N., et al. 2016, *A&A*, 594, A13  
 Prochaska, J. X., Tejos, N., Crighton, N., et al. 2017a, Linetools/Linetools: Third Minor Release, v0.3, Zenodo, doi:10.5281/zenodo.1036773  
 Prochaska, J. X., Tejos, N., cwotta, et al. 2017b, Pyigm/Pyigm: Initial release for publications, v1.0, Zenodo, doi:10.5281/zenodo.1045479  
 Prochaska, J. X., Werk, J. K., Worseck, G., et al. 2017, *ApJ*, 837, 169  
 Rubin, K. H. R., Prochaska, J. X., Koo, D. C., et al. 2014, *ApJ*, 794, 156  
 Saintonge, A., & Catinella, B. 2022, *ARA&A*, 60, 319  
 Schiminovich, D., Wyder, T. K., Martin, D. C., et al. 2007, *ApJS*, 173, 315  
 Stocke, J. T., Penton, S. V., Danforth, C. W., et al. 2006, *ApJ*, 641, 217  
 Tchernyshyov, K., Werk, J. K., Wilde, M. C., et al. 2023, *ApJ*, 949, 41  
 Tejos, N., Prochaska, J. X., Crighton, N. H. M., et al. 2016, *MNRAS*, 455, 2662  
 Tumlinson, J., Peeples, M. S., & Werk, J. K. 2017, *ARA&A*, 55, 389  
 Tumlinson, J., Thom, C., Werk, J. K., et al. 2011, *Sci*, 334, 948  
 Tumlinson, J., Thom, C., Werk, J. K., et al. 2013, *ApJ*, 777, 59  
 Virtanen, P., Gommers, R., Oliphant, T. E., et al. 2020, *NatMe*, 17, 261  
 Werk, J. K., Prochaska, J. X., Thom, C., et al. 2012, *ApJS*, 198, 3  
 Werk, J. K., Prochaska, J. X., Thom, C., et al. 2013, *ApJS*, 204, 17  
 Werk, J. K., Prochaska, J. X., Tumlinson, J., et al. 2014, *ApJ*, 792, 8  
 Zahedy, F. S., Chen, H.-W., Johnson, S. D., et al. 2019, *MNRAS*, 484, 2257  
 Zheng, Y., Faerman, Y., Oppenheimer, B. D., et al. 2024, *ApJ*, 960, 55